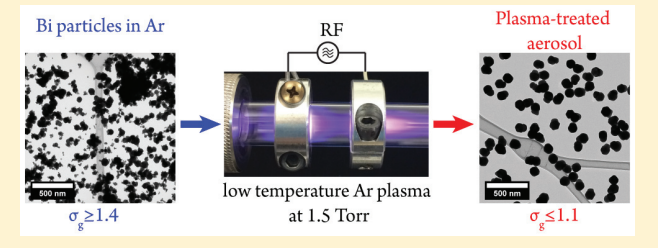
In-Flight Size Focusing of Aerosols by a Low Temperature Plasma

Necip B. Uner[†] and Elijah Thimsen*,^{†,‡}

[†]Department of Energy, Environmental and Chemical Engineering, and [‡]Institute for Materials Science and Engineering, Washington University in St. Louis, 1 Brookings Dr., St. Louis, Missouri 63130, United States

Supporting Information

ABSTRACT: Thermodynamics dictate the direction of all chemical and physical processes. In the case of aerosols, maximization of entropy leads to a broadening of the size distribution as the system proceeds toward equilibrium. The expectation is that as an aerosol ages, the size distribution will broaden. Contrary to this expectation, in this work we demonstrate that the unique nonequilibrium environment in a low temperature plasma can modify particulate materials to make the size distribution narrower. Submicrometer aerosols



composed of bismuth particles with a polydispersed size distribution were prepared and passed through a low temperature argon plasma. For lower powers at which the plasma operated near room temperature, the incoming polydispersed aerosol was converted into a monodispersed aerosol of geometric standard deviation approximately 1.1 with 65% mass yield. The mechanism by which the process took place involved the particles vaporizing in the plasma operating at near room temperature, which resulted in very large supersaturation of metal vapor. Particle heating and sputtering by ion bombardment are discussed as possible mechanisms leading to vaporization that causes the change in the size distribution to make it narrower.

INTRODUCTION

Gas phase synthesis methods earned their credit by providing high-throughput production of various nanomaterials, including oxides, metals, and metal alloys. 1-3 These methods involve feeding a liquid or vapor precursor into a high temperature medium, a flame, or a hot wall reactor, for example, which thermally activates particle growth. A hot environment provides rapid precursor conversion and particle nucleation. Following this step, equilibrium favors growth by agglomeration; thereby it is common to form hard aggregates. 4,6,7 As time proceeds, the size distribution of the aggregates broadens, and its geometric standard deviation, σ_{g} , usually approaches the self-preserving value of 1.3 if sintering is rapid.^{6,8} The difficulties in size control, monodispersity, and shape stand out as drawbacks of gas phase synthesis methods when compared to colloidal synthesis.

In the past 10 years, low temperature plasma (LTP) has been explored as an alternative to thermal processing. Interestingly, particles produced by LTP often have a monodispersed size distribution and are crystalline. In a LTP, particles are bombarded by mobile electrons having high kinetic energy and most particles become negatively charged. The Coulombic repulsion arising between these unipolar charged particles suppresses coagulation^{9,10} and has been used to explain the resultant monodispersed size distribution for vapor-to-solid conversion processes. Figure 1 compares the aerosol dynamics in vapor-fed thermal processing to processing based on LTP. High quality nanocrystals of silicon, 11 germanium, 12 oxides, 13 and sulfides 14 have been produced using LTPs. Few reports on synthesis of metal particles also exist.15

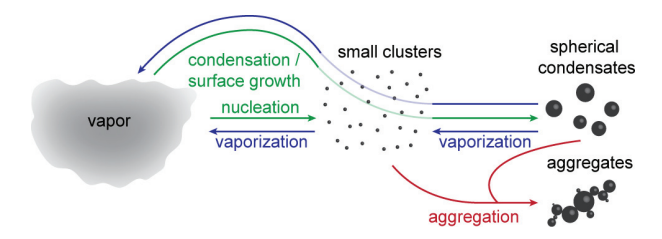


Figure 1. Aerosol dynamics in vapor-to-solid gas-phase processes. Blue arrows show pathways exclusive to LTPs. Steps shown by red arrows are relatively absent in LTPs but prominent in thermal media. Steps in green are seen in both thermal media and LTPs.

LTPs constitute a nonequilibrium environment that contains very hot electrons (approximately 10 000 K < T_e < 50 000 K) and cold neutral gas molecules and ions that are typically near room temperature. Because of this nonequilibrium environment, LTPs have the potential to modify chemical and physical kinetics in unique ways. This feature of LTPs inspired the concept of the "processor". ¹⁶ A processor takes electrical work as an input and acts upon an amount of mass to alter its configuration. Ideally, the processor can be designed so that the nonequilibrium environment contained within it converts an undesired form of mass into a desired form. This can happen either by chemical or physical steps, which may be forbidden or extremely slow in thermal routes governed by local equilibrium.

Received: April 15, 2017 Revised: May 28, 2017 Published: June 7, 2017

In this work, we demonstrate that LTPs can function to process a premade aerosol by a simple experiment. Submicrometer aerosols of metallic bismuth with a polydispersed size distribution were produced upstream by a thermal route using an evaporation-condensation generator and subsequently passed through a capacitively coupled radio-frequency (RF) argon plasma downstream which acted as the processor. A digital image of the plasma during operation is presented in Figure S1. The desired form of the size distribution is monodispersed, and it was found that the plasma can convert a polydispersed size distribution into a size distribution with geometric standard deviation less than or equal to 1.1, which is an accepted indicator of monodispersity for gas-phase synthesized particulate materials. 17 The observed transformation in size distribution requires a new mechanism in the growth dynamics of particulate materials in LTP, namely, vaporization at low temperature by a nonequilibrium process. We argue that either particle heating or sputtering due to ion bombardment can explain the observed vaporization. The vaporization mechanism presented here, which operates in a highly nonequilibrium environment, is expected to assist a wide range of chemical transformations during synthesis of materials in LTPs, and it may be a major reason for the production of monodispersed particles in LTPs.

METHODS

Experimental Setup. The test aerosol was generated by an evaporation—condensation process (Figure 2). In this method,

Aerosol generator Low temperature plasma Pressure Removable Diagnostic port gauge Excess collection - Axial OES to exhaust RF filter or - Langmuir probe \odot TEM grid - Temperature probe **0**° Furnace vacuum Forced Radial OES gump

axial position

Figure 2. Experimental setup. Gas flow is from left to the right.

a thermal medium evaporates the material. The produced vapor is carried by an inert gas, and the vapor—gas mixture is then rapidly quenched, leading to aerosol growth. By adjusting the temperature of the evaporating medium and the quenching rate, it is possible to generate aerosols having different size distributions and mass concentrations. The method allows synthesis of materials without using metal—organic vapor precursors. Precursors were avoided to study plasma—particle interaction in a well-defined environment that contains no chemicals other than the particle material and the plasma gas.

Bismuth was selected as the material since it is relatively easy to generate an aerosol of it by evaporation—condensation. Pellets of Bi (Sigma-Aldrich), weighing approximately 33 g, were placed into an alumina boat. The boat rested in a fused silica tube of 1.9 cm outer diameter, and the tube was placed into a furnace (CM Furnaces Inc., Bloomfield, NJ). The carrier gas was ultrahigh purity argon (Praxair UHP 5.0), and it flowed through the tube at a rate of 5000 sccm, which was controlled using a mass flow controller (G-Series MKS, Andover, MA). By operating the furnace at 900 and 1000 °C, two different

aerosols were created upon subsequent quenching. These aerosols had different mass concentrations. The aerosol generated using a furnace temperature of 900 °C had a mass concentration of 0.54 mg m⁻³ and is termed low concentration. The aerosol generated at 1000 °C had a mass concentration of 2.7 mg m⁻³ and is termed high concentration. Over the course of a single experiment, approximately 10% of the Bi evaporated from the boat. Quenching of the vapor was accomplished using an electric fan to increase the cooling rate by forced convection over a portion the tube that was approximately 28 cm in length. The test aerosols were found to be very reproducible for runs on different days for the same process parameters (Figure S2). Downstream from the evaporation/condensation generator, a portion of the aerosol was sampled through a 150 μm tube orifice (SS 1/4 in. optically measured, Lenox Laser, Glen Arm, MD) into a low-pressure section, wherein the plasma was generated. The pressure was maintained at 1.5 Torr using a diaphragm valve upstream of the rotary vane vacuum pump and measured using a pressure transducer (Baratron MKS, Andover, MA). At the inlet to the vacuum section, the temperature was measured by a K-type thermocouple and found to be approximately 22 °C. The gas velocity in the vacuum portion of the apparatus was approximately 7.4 m s⁻¹. The plasma was generated in a fused silica tube of 1.9 cm outer diameter and 1 mm wall thickness by capacitively coupling RF power through two aluminum ring electrodes. The powered electrode was upstream of the ground electrode. The position of the electrodes was kept fixed in all experiments. A 13.56 MHz RF power supply (AG0613, T&C Power Conversion, Rochester, NY) was used in conjunction with a matching network (AIT600, T&C Power Conversion, Rochester, NY) to minimize the reflected power. For all RF powers used (10-120 W), the plasma filled the entire silica tube (Figure S1).

Electron Microscopy. Particles were collected upstream of the diaphragm valve for imaging with a transmission electron microscope (TEM). The particles were dispersed on an ultrathin carbon film, which was supported on lacey carbon, which in turn was supported on a copper grid. The TEM grids were suspended vertically on a 400-mesh steel filter using adhesive tape. Particles were found to deposit on the center of the filter at low input plasma powers, up to 40 W. Thus, the TEM grids were placed in the center of the filter for experiments conducted with low RF power inputs. At higher powers the deposition pattern was observed to expand on the filter in the form of a concentric ring. Experiments were conducted wherein TEM grids were placed at different radial positions on the filter, and it was found that there was negligible particle deposition outside of the observed rings. For subsequent experiments at higher RF power inputs, the grid was placed in the ring wherein the particles deposited. The collected particles were imaged with a TEM having a 120 kV LaB₆ filament (Tecnai G2 Spirit, FEI, Hillsboro, OR). Primary particle sizes were extracted by processing the images with ImageJ software. A minimum of 260 particles were counted from the images obtained from each grid. Histograms were created for the frequency distribution of the logarithm of primary particle diameter. Normal distributions were fitted to these histograms. The corresponding geometric standard deviations (σ_g) of a log-normal distribution, which is frequently used to characterize aerosols, was obtained with the formula $\sigma_{
m g}$ = $e^{2.303\sigma}$, where σ is the standard deviation for the normal distribution fitted to the histogram of the logarithm of particle diameter. Monodispersed is defined as $\sigma_{\rm g} \leq 1.1.^{17}$

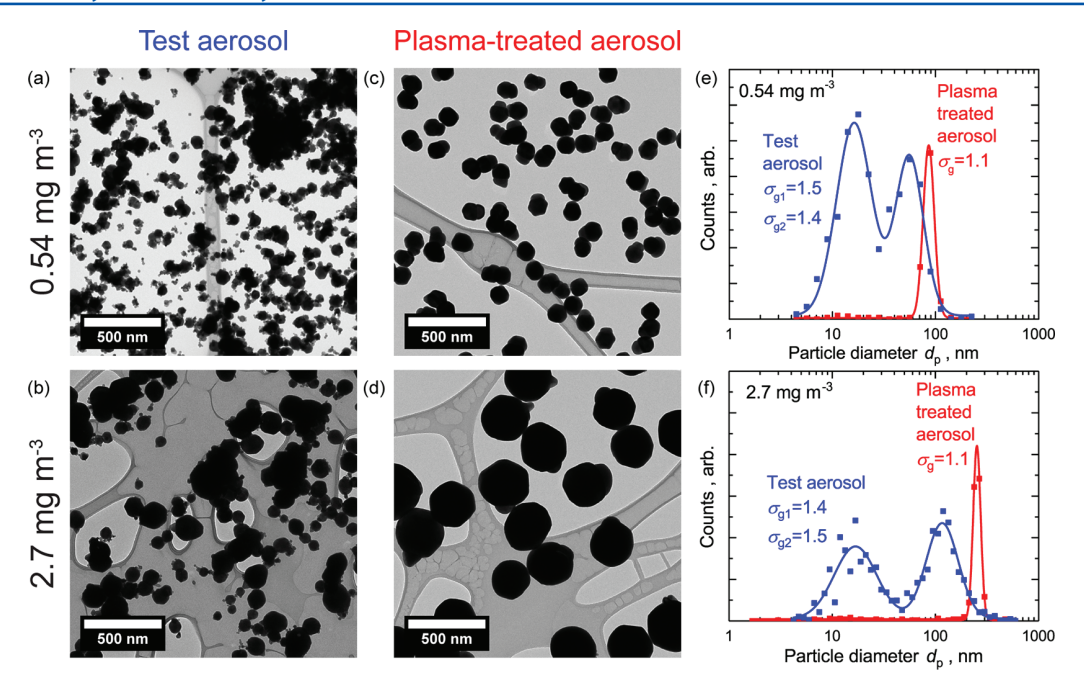


Figure 3. (a, b) Bismuth test aerosols at different mass concentrations, termed respectively as low concentration and high concentration in the text. (c, d) Plasma treated forms of the aerosols given in (a) and (b) at 10 and 20 W of applied RF power, respectively. (e, f) Frequency distribution of primary particle size for aerosols of low and high concentration, with plasma off and on. Fitted curves represent log-normal distributions and corresponding geometric standard deviations are given.

Plasma Treatment of Aerosols. Test aerosols were treated with the plasma at different input powers. For the low concentration aerosol, the upper limit was 40 W. For the high concentration aerosol, the maximum power explored was 120 W. Powers lower than 10 W were not investigated.

Mass yield of the plasma treatment was assessed by collecting particles on filters upstream of the diaphragm valve. Four hundred mesh stainless steel filters were used. These stainless steel mesh filters were found to have very high collection efficiency. For mass measurements, only the high concentration aerosol was used in order to collect more material and make the measurements more accurate.

Optical Emission Spectroscopy (OES). Light emitted from the plasma was collected by a fiber-optic cable connected to a positive lens. Intensities over the spectrum between 200 and 1025 nm were measured using a spectrometer equipped with a linear silicon CCD array detector (USB2000+XR1-ES, Ocean Optics, Dunedin, FL). Light was collected using two different configurations. In the first configuration, the lens was placed below the fused silica tube. The emission spectra were recorded at different axial positions along the plasma. In the second configuration, the lens was placed at the diagnostic port at the end of the straight tubular path and aligned with the axis of the plasma tube (Figure 2).

Plasma Parameters. A Langmuir double probe (Impedans LTD, Dublin, Ireland) was used to measure the ion density and electron temperature. Platinum tips of 5 mm length and 0.19 mm diameter were used. Measurements were done in the absence of particles to minimize interference from material deposited on the probe surface.

A fiber-optic temperature probe (OptoTemp 2000 Super Probe, Micromaterials Inc., Tampa, FL) was used to obtain an estimate of the gas temperature inside the plasma. The sensor operates on the basis of fluorescence decay of a phosphor located at the tip of the probe. ¹⁹ Since surfaces immersed in the

plasma get hotter than the ambient gas (vide infra), the temperatures measured with the probe indicate a maximum for the gas temperature.

■ RESULTS AND DISCUSSION

Electron microscopy revealed that the size distribution of the test aerosols became narrower after they passed through the plasma (Figure 3). Initially polydispersed aerosols (Figure 3a,b) became monodispersed after plasma treatment, if the power was sufficiently low-10 and 20 W respectively for the low and high concentration aerosols (Figure 3c,d and Figure S3). For both test aerosols, which had different mass concentrations and frequency distributions, the geometric standard deviation approached 1.1. The mean sizes of the number distributions were seen to be larger after plasma treatment (Figure 3e,f). As input powers increased, the monodispersed peak started to vanish while its mean size increased and the fine mode reappeared (Figures S4 and S5). When input powers were high enough, an aerosol similar to the test aerosol was observed; however, the mass concentration was much less than the test aerosol. The mass yield decreased rapidly as input powers increased, presumably as a result of wall losses. A metallic film downstream of the powered electrode was quickly deposited at high power inputs and observed after sufficiently long experiments at lower power (Figure S6). Thus, it was found that if properly tuned, the LTP was clearly capable of acting as a processor to focus the size of the aerosol.

At the plasma conditions that produced the monodispersed size distribution, the fiber-optic temperature probe was inserted into the center of the powered electrode to estimate the gas temperature. The temperature measured by the sensor was 81 and 135 °C for 10 and 20 W input power, respectively. These values are upper limits for the gas temperature, since ion bombardment is expected to heat the probe. Temperature measurements indicate that the plasma is far from thermal-

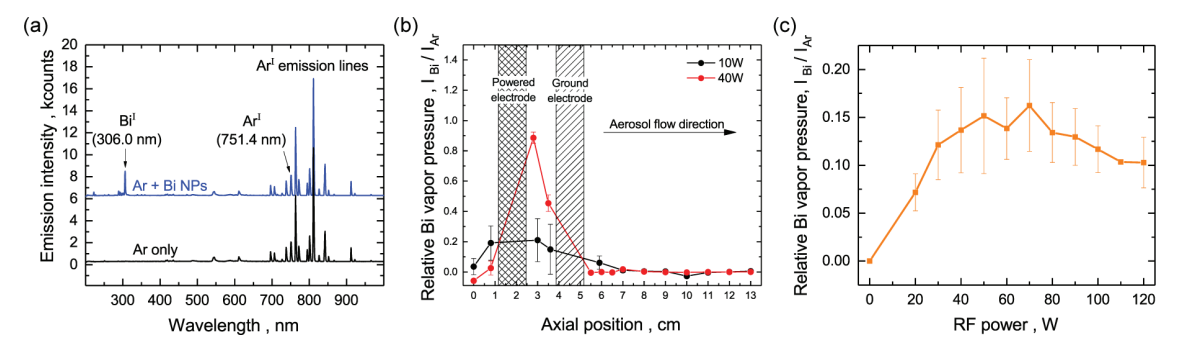


Figure 4. (a) Emission spectra gathered downstream of the powered electrode with and without particles. The upper spectrum is offset for clarity. (b) Bismuth actinometry obtained from the peaks given in (a). *I* is the intensity. The data are obtained as a function of position along the cylindrical axis of the plasma with the low concentration test aerosol. (c) Axially integrated actinometry at different powers obtained with the high concentration test aerosol.

ization. Consequently, nonequilibrium growth dynamics, such as vaporization despite the low gas temperature, are expected.

Unipolar negative charging of the aerosol particles in the LTP cannot fully explain the observation that the plasma causes the polydispersed aerosol to become monodispersed, since mass is being redistributed among different bins in the size distribution. However, if a new mechanism is included whereby particles can vaporize to generate a highly supersaturated vapor, despite the low gas temperature, then it would be possible to generate a monodispersed size distribution by condensation onto nuclei and remaining fragments. Such a mechanism has previously not been considered for low temperature plasmas. If vaporization of the Bi were occurring in the low temperature plasma, then we expect to observe photoemission from excited electronic transitions in those free Bi atoms. Optical emission spectroscopy (OES) measurements revealed that the Bi particles did indeed vaporize in the plasma, despite the low gas temperature. Figure 4a shows the OES spectra for a representative plasma with and without Bi particles present. The highest Bi peak observed at 306.0 nm belonged to the documented $6p^2(^3P_0)7s \rightarrow 6p^3$ transition at 306.77 nm. ²⁰ At all power inputs, there was clear emission from atomic Bi when the particles were sent into the plasma. The Bi vapor detected by OES resulted from particle vaporization and was not residual vapor from the evaporation-condensation particle generator (Supporting Information). Actinometry²¹ was performed by taking the ratio of the main Bi emission line to a neutral Ar emission line (Supporting Information). The Ar^I line at 751.4 nm was selected $(3s^23p^5(^2P^{\circ}_{3/2})4p \rightarrow 3s^23p^5(^2P^{\circ}_{3/2})4s)$. The change in the magnitude of the Ar I line used for actinometry was found to be small in the presence of particles. Actinometry revealed that the Bi vapor was produced and lost in the vicinity of the powered electrode (Figure 4b). The vapor appeared upstream of the powered electrode and vapor content increased as particles approached this electrode. Just downstream of the powered electrode, the vapor content reached a maximum, but then it rapidly vanished at positions further downstream, even though the plasma still occupied that space (Figure S1). At 10 W, the power which resulted in the monodispersed output for the low concentration aerosol, vaporization was gradual and reached a plateau inside the powered electrode. At 40 W, vaporization was much more intense. The observation of Bi vapor by OES, which must by highly supersaturated given the low gas temperature, is consistent with the rapid deposition of the metal film on the wall of the plasma tube (Figure S6).

The rate of film deposition on the walls of the plasma tube was very fast with the high concentration aerosol. Therefore, the lens was placed at the diagnostic port downstream and oriented such that light was integrated along the cylindrical axis of the system (Figure 2). Using this configuration, information about the distribution of Bi vapor along the cylindrical axis of the plasma was lost; however, it was possible to estimate the total relative Bi vapor content within the plasma, since the integrated intensities of the selected lines for Bi and Ar were obtained (Supporting Information). As shown in Figure 4c, the total vapor content increased with increasing power input. At approximately 70 W, the total vapor content did not increase with further increases in applied RF power, indicating complete vaporization. At higher powers, the vapor content decreased slightly, which can be explained by increased losses to the walls. From the OES results, the particles were clearly being vaporized in the plasma, despite the low gas temperature.

The mass yield of the process decreased with increasing power (Figure 5a). For the high concentration case at 20 W, which was the power that resulted in the monodispersed size distribution in Figure 3d, the mass yield was found to be 65%. Mass losses increased with increasing power and for powers larger than 60 W very little mass was collected.

By assuming the particles were spherical, the mass measurements allow quantitative mass distributions to be established. The properties of the distributions are given in Table 1 (also Figure S7 for all measurable powers). In comparison to the size distributions given in Figure 3, mass distributions in Figure 5b clearly show the transport of mass from both sides of the size spectrum. For the monodispersed case at 20 W with the high concentration aerosol, it can be seen from Figure 5b that the amount of mass in the size range of the monodispersed peak after plasma treatment was greater than the amount of mass in that size range for the test aerosol. Accordingly, this mass transport resulted in the disappearance of particles that were larger and smaller than the final size. This type of a transformation indicates that all particles vaporize. Therefore, an overall growth mechanism similar to Ostwald ripening, during which the vapor generated from small particles recondense on the stable large particles, is unlikely.

Before developing a model to describe the aerosol dynamics occurring in the plasma, ion density and electron temperature must be measured. From Langmuir double probe measurements, the ion density was found to increase with plasma power and vary with axial position. The orders of magnitude of our measurements agree with previous characterization of RF Ar

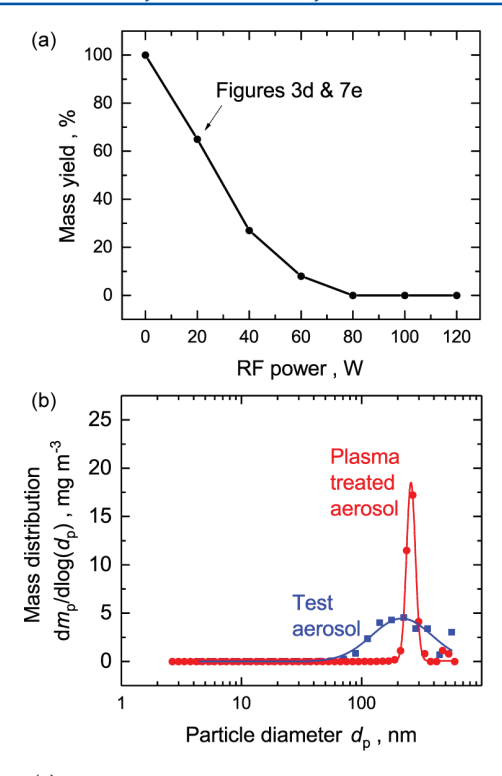


Figure 5. (a) Mass yield as a function of applied RF power for the high concentration aerosol. (b) Mass distribution of high concentration aerosol before and after plasma treatment at 20 W input power.

Table 1. Properties of the Low Concentration (LC) and High Concentration (HC) Test Aerosols along with the Plasma Treated Forms of the High Concentration Aerosol^a

	$d_{ m p,1} \choose m nm)$	$\binom{d_{\mathrm{p,2}}}{(\mathrm{nm})}$	$m_{\rm f} \ (\mu { m g/min})$	$N_{\infty}~(\mathrm{m}^{-3})$	$\frac{M_{\infty}}{(\text{mg/m}^3)}$
LC, plasma off	16	56	48	8.72×10^{11}	0.54
HC, plasma off	17	116	242	2.62×10^{11}	2.69
HC, 20 W		251	166	2.27×10^{10}	1.78
HC, 40 W	148	341	70	4.88×10^{9}	0.73
HC, 60 W	17	249	20	4.17×10^{9}	0.22

^aThe variable $d_{\rm p,1}$ is the mean size of the finer mode, $d_{\rm p,2}$ is the mean size of the coarse mode, $m_{\rm f}$ is the mass flow rate of particles, N_{∞} is the total number concentration, and M_{∞} is the total mass concentration.

glow discharges in vessels of similar size.²² The ion density and electron temperature, measured in the center of the powered electrode, are plotted as a function of applied RF power in Figure 6a. The ion density increased with applied RF power in the range from $\sim 2 \times 10^{17}$ to 2×10^{18} m⁻³. The average electron temperature was approximately 4 ± 1.5 eV. This value did not change significantly as a function of power or axial position. The ion density, however, was found to change with axial position. Ion density as a function of axial position for an applied RF power of 20 W is plotted in Figure 6b. There was a region of high ion density in the powered RF electrode, and immediately upstream, which is shaded red in Figure 6b. Downstream of the powered electrode, the ion density rapidly decreased. The region of low ion density downstream of the powered electrode is shaded blue in Figure 6b. There was plasma in the low ion density region (Figure S1), but it was less intense than the high ion density region. A similar trend was seen in the Ar^{II} emission measured by OES (data not shown).

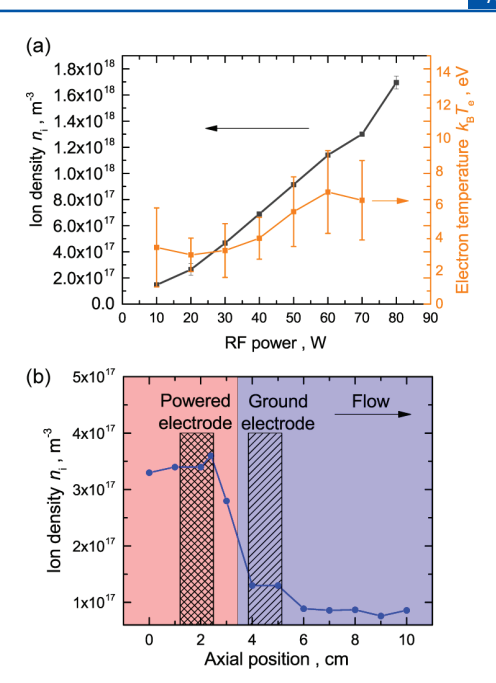


Figure 6. (a) Ion density and electron temperature at the center of the powered electrode as a function of RF power. (b) Axial distribution of ion density in the vicinity of the powered electrode at 20 W.

Therefore, the flow-through LTP is envisioned as a two-zone system. From Figure 4b, the absence of vapor in the plasma downstream of the ground electrode is an indication that any vaporization or condensation processes were complete before the gas exited the portion of the tube upstream of the ground electrode. The residence time in the region of the plasma upstream of the ground electrode was approximately 10 ms. In the weaker plasma downstream of the intense plasma, particles are thought to have a unipolar charge and suppressed coagulation. Therefore, the 10 ms time frame in the intense plasma is expected to be responsible for the changes in the size distribution of the aerosol. Given these experimental observations, the system can be modeled by including the additional vaporization mechanism (Figure 1) and by treating it as two zones in series with different ion densities. Before the system can be modeled, first a description of the vaporization mechanism must be developed. With known aerosol and plasma parameters, possible vaporization mechanisms can be described quantitatively. The mechanism must allow vaporization amidst a gaseous atmosphere close to room temperature. Two possibilities are thermal evaporation due to particle heating and sputtering. First, we address thermal evaporation due to particle heating, and then we will address sputtering.

It has been experimentally shown that particles inside a plasma are heated to temperatures higher than that of the surrounding gas.^{23–25} This heating is caused by ion and electron bombardment of the negatively charged particles. Upon bombardment, ions recombine with electrons and transfer a part of their kinetic energy. The energy released upon ion neutralization is believed to be a major driver of particles being heated in LTP to a temperature above the gas temperature.²⁶ In our system, the particle temperature is expected to be nominally independent of size for particles larger than 10 nm in diameter. Calculating the particle temperature requires a particle charging model, since ion fluxes, which depend on particle charge, must to be calculated

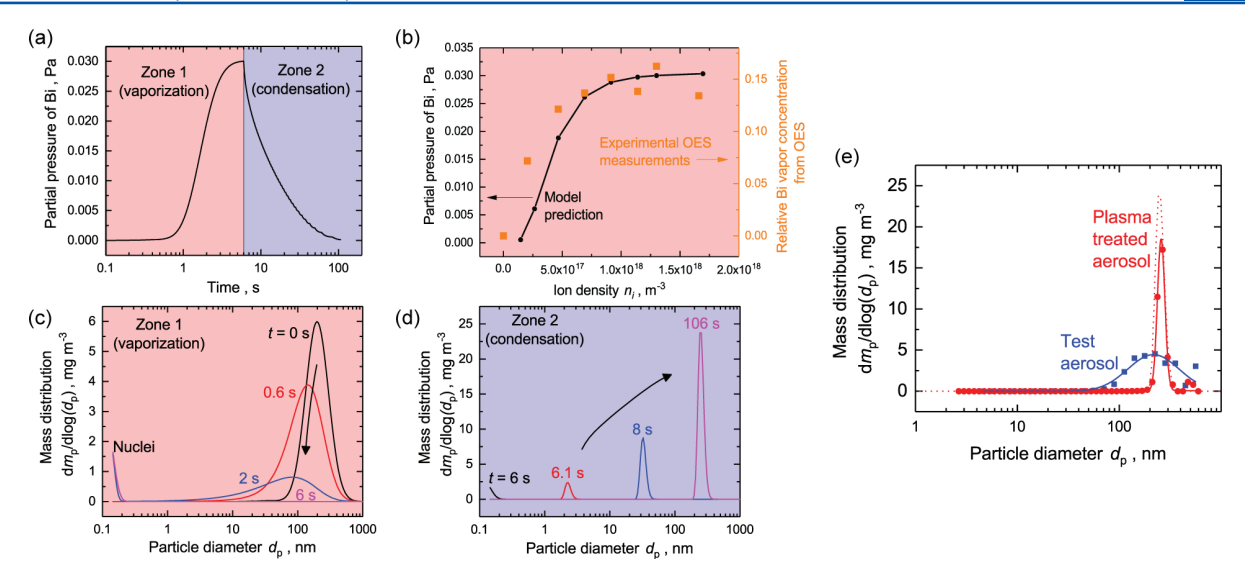


Figure 7. (a) Calculated bismuth partial pressure as a function of time in a plasma having an ion density $n_i = 1.7 \times 10^{18} \text{ m}^{-3}$ in zone 1, with the high concentration test aerosol. (b) Calculated partial pressure of Bi in the vaporization zone compared with the experimental data presented in Figure 4c. (c, d) Evolution of the size distribution during vaporization and condensation using the same parameters as (a). (e) Experimental (solid) and model (dotted) results of the mass distribution before and after plasma treatment.

(Supporting Information). Orbital motion limited (OML) theory is the simplest and one of the most commonly used theories for predicting particle charges when the sheath around the particles is collisionless for ions. OML theory predicts particle temperatures approximately equal to 240 °C at 20 W (Supporting Information). At such temperatures, bismuth particles have negligible vapor pressure irrespective of their size. However, more recent theories, such as the collisionenhanced model (CEM), 28-30 predict different results. The collision-enhanced model also evaluates the ion-neutral collisions occurring in the vicinity of the particle. These collisions increase ion flux to the particle but in turn decrease ion bombardment energy. Overall, CEM predicts higher recombination rates and hotter particles. CEM predicts temperatures above 600 °C, at which the vapor pressure of Bi is significant. The choice of charging model controls whether particle heating can explain the experimental observation or

Sputtering is an alternative means by which particles could be vaporized in the LTP at room temperature, but its quantitative description also presents some difficulties. Using OML theory and the measured plasma parameters, the particle potential with respect to the plasma, Φ_{p} , can be calculated. The negative potential of the particle accelerates ions, which impact with an energy that can be estimated as $e|\Phi_p|$, e being the elemental charge. Ion bombardment energies are calculated to be approximately 6.4 eV in our LTP. Such ion energies are significantly larger than the surface binding energy of bismuth, which is 1.9 eV when calculated from the enthalpy of sublimation. In the classical theory of sputtering, yields for such ion energies are very low.³¹ However, sputtering theories and empiricisms are mostly developed for large planar surfaces, not for charged particles with a curved surface. Such particles are expected to have lower surface binding energies and increased sputtering yields. 32,33 It is interesting to note that sputtering is much less affected by the selection of charging theories. While OML theory predicts large ion energies and smaller ion fluxes to the surface, CEM asserts lower ion energies but higher ion flux, somewhat balancing to result in a

similar sputtering rate. In general, the rate of vaporization by sputtering can be expressed as

$$SR = \frac{J_i Y}{e n_{at}} \tag{1}$$

where I_i is the ion flux predicted by either OML theory or CEM, Y is the sputtering yield, and $n_{at} = \rho/MW$ is the atomic density with ρ being the density and MW being the molecular weight. SR has the units of length per time. The sputtering yield can be estimated by various semiempirical formulas for the near-threshold regime. 31,34 Like vaporization by heating, sputtered atoms lead to the generation of a supersaturated vapor around the particles due to low gas temperatures. This vapor condenses back onto available nuclei and fragments. The process of condensation can be described with kinetic theory since particle Knudsen numbers in our system, $Kn = 2\lambda/d_p$ with λ being the mean free path of gas atoms, are much greater than 10.35 Using eq 1, the new vaporization mechanism occurring in the LTP can be incorporated into established models of aerosol dynamics, and the predicted final size distributions can be compared with the experimental results.

Based on the descriptions of aerosol charging, condensation, and vaporization discussed above, an aerosol dynamics model was constructed to track the evolution of the size distribution within the plasma (see Supporting Information for details). Sputtering was selected as the vaporization mechanism. The size distribution was obtained by solving the Liouville equation, which is a transport description of growth and shrinkage in particle size space. The model also calculates the Bi vapor pressure, which can be compared to the experimental OES measurements. To compensate for the uncertainties in the sputtering yield, the model was run for sufficient time in the intense zone until the vapor pressure reached a nominally steady state value. The vapor pressure of Bi calculated by the model reproduced the OES data surprisingly well as a function of the measured ion density (Figure 7a). After this step of intense vaporization, both the vapor and the remaining particles enter the less intense zone with reduced ion density. In the less intense zone, the sputtering rate was insufficient to maintain the large supersaturation of Bi vapor that was developed in the first zone. A nucleation burst occurred, and the Bi vapor began to condense. Since the nuclei were monodispersed, the size distribution remained nominally monodispersed as the vapor condensed onto them. As the material moved further downstream, condensation proceeded to completion (Figure 7b). The size distribution of the aerosol as a function of time in the two zones of different ion density are given in Figures 7c and 7d. It should be noted that the size distribution broadens during vaporization. Therefore, to obtain a final distribution that is narrower than the initial distribution by recondensation, the majority of the aerosol must be vaporized.

The resulting mass distribution was closely captured by the model (Figure 7e). The overpredicted amount of mass in the monodispersed size is due to the omission of vapor losses. Interestingly, the plasma provided much faster kinetics than the model predicted. The time scale necessary for good resemblance between the size distribution predicted by the model and the experimental result is orders of magnitude larger than the experimental time scale. The discrepancy during vaporization may be caused by of the omission of surface charge effects and surface curvature in the classical theory of sputtering yield. Of course, the other option is that particle heating may be the more important vaporization process. The mismatch between model and experiment in the time scales of condensation is possibly due to higher local vapor concentrations because of vapor ionization³⁶ and particle confinement effects.^{37,38} Future work will focus on including these phenomena and deconvolution of the vaporization mechanisms.

CONCLUSION

It has been shown that low temperature plasmas can be used to transform polydisperse aerosols into significantly more monodisperse aerosols. It has been demonstrated that the mechanism inducing this polydisperse-to-monodisperse transformation is vaporization. The highly supersaturated vapor produced by ion bombardment condenses on the small clusters and nuclei and the particles grow as monodispersed. A similar overall mechanism is expected for treatment of aerosols comprising refractory materials, only that these materials are expected to vaporize at larger power inputs.

According to the Langmuir probe measurements and model results, ion densities were greater than particle number densities except during entry to the less intense zone. Apart from this very brief period, during which sub-nanometer particles were created due to the nucleation burst, coagulation was suppressed. ¹⁰ Unipolar negative charging prevented collisional broadening of the size distribution.

The lack of coagulation is a key difference between the LTP and a two-zone process that one might imagine using a thermal system. Another key difference is that the physical steps of aerosol dynamics in LTPs are reversible (Figure 1). The reversibility along with rapid kinetics brings flexible ways of processing materials if the plasma parameters, for example, electron energy distribution and ion density, are properly tuned.

Describing the vaporization mechanism provides numerous challenges. Nevertheless, understanding the dynamics is crucial to controlling the final particle size. Independent of the mechanism that causes vaporization, the nucleation rate is expected to be important since it determines the final

monodispersed size of the particles. For a given amount of supersaturated vapor, a faster nucleation rate would result in smaller particles, while a slower nucleation rate would give larger particles. The vapor generated from refractory materials is anticipated to yield smaller particles due to faster nucleation, since refractory materials have low equilibrium vapor pressures. Adjustment of input aerosol concentrations, operating power, optimization of plasma geometry, and manipulating the vapor amounts can make LTPs an effective size processing tool for gas-phase synthesized nanomaterials.

From the perspective of thermodynamics, LTP allows one to put work into the system, which can lead to a transformation resulting in monodispersed size distribution. It is important to note that this work input is different than filtering out certain portions of the size distribution. The LTP takes mass from across the size distribution and transports it into the final monodispersed size. Thus, the LTP has a much higher throughput of mass compared to other approaches for obtaining monodispersed size such as electrostatic classification.^{39–41} It is interesting to note that such a transformation in the size distribution cannot occur spontaneously. It is wellknown that particulate media tend to decrease surface energy by means of coagulation in the case of aerosols or via Ostwald ripening in the case of colloids. The decrease in surface area and surface energy is accompanied by an increase in entropy until equilibrium has been reached. Coagulation and Ostwald ripening lead to a broadening of the size distribution. 42,43 The spread of the size distribution is a measure of the specific entropy of an aerosol44 (Supporting Information), and it increases monotonically during coagulation. Interestingly, by narrowing of the size distribution, the LTP appears to have decreased the specific entropy of the aerosol.

ASSOCIATED CONTENT

S Supporting Information

The Supporting Information is available free of charge on the ACS Publications website at DOI: 10.1021/acs.jpcc.7b03572.

Pictures of the experimental setup, additional size distributions, additional information on the OES measurements, the particle heating model, details about the aerosol dynamics calculations and specific entropy of the particle size distribution (PDF)

AUTHOR INFORMATION

Corresponding Author

*E-mail elijah.thimsen@wustl.edu; Tel +1.314.935.6103 (E.T.).

ORCID

Elijah Thimsen: 0000-0002-7619-0926

Notes

The authors declare no competing financial interest.

ACKNOWLEDGMENTS

The authors thank the School of Engineering and Applied Sciences at Washington University in Saint Louis, I-CARES (International Center for Advanced Renewable Energy & Sustainability), and the University Strategic Research Alliance for financial support. This work was performed in part at the Nano Research Facility (NRF) at Washington University in Saint Louis.

ABBREVIATIONS

LTP, low temperature plasma; RF, radio frequency; TEM, transmission electron microscopy; OES, optical emission spectroscopy; OML, orbital motion limited; CEM, collision-enhanced model.

REFERENCES

- (1) Swihart, M. T. Vapor-Phase Synthesis of Nanoparticles. *Curr. Opin. Colloid Interface Sci.* **2003**, *8*, 127–133.
- (2) Hahn, H. Gas Phase Synthesis of Nanocrystalline Materials. *Nanostruct. Mater.* **1997**, *9*, 3–12.
- (3) Vollath, D. Plasma Synthesis of Nanopowders. J. Nanopart. Res. 2008, 10, 39-57.
- (4) Strobel, R.; Pratsinis, S. E. Flame Aerosol Synthesis of Smart Nanostructured Materials. *J. Mater. Chem.* **2007**, *17*, 4743–4756.
- (5) Fu, J.; Daanen, N. N.; Rugen, E. E.; Chen, D. P.; Skrabalak, S. E. Simple Reactor for Ultrasonic Spray Synthesis of Nanostructured Materials. *Chem. Mater.* **2017**, *29*, 62–68.
- (6) Friedlander, S. K. Smoke, Dust, and Haze: Fundamentals of Aerosol Dynamics, 2nd ed.; Oxford University Press: New York, 2000.
- (7) He, Y.; Li, X.; Swihart, M. T. Laser-Driven Aerosol Synthesis of Nickel Nanoparticles. *Chem. Mater.* **2005**, *17*, 1017–1026.
- (8) Teoh, W. Y.; Amal, R.; Mädler, L. Flame Spray Pyrolysis: An Enabling Technology for Nanoparticles Design and Fabrication. *Nanoscale* **2010**, *2*, 1324–1347.
- (9) Kortshagen, U. R.; Sankaran, R. M.; Pereira, R. N.; Girshick, S. L.; Wu, J. J.; Aydil, E. S. Nonthermal Plasma Synthesis of Nanocrystals: Fundamental Principles, Materials, and Applications. *Chem. Rev.* **2016**, *116*, 11061–11127.
- (10) Kortshagen, U.; Bhandarkar, U. Modeling of Particulate Coagulation in Low Pressure Plasmas. *Phys. Rev. E: Stat. Phys., Plasmas, Fluids, Relat. Interdiscip. Top.* **1999**, *60*, 887–898.
- (11) Mangolini, L.; Thimsen, E.; Kortshagen, U. High-Yield Plasma Synthesis of Luminescent Silicon Nanocrystals. *Nano Lett.* **2005**, *5*, 655–659
- (12) Gresback, R.; Holman, Z.; Kortshagen, U. Nonthermal Plasma Synthesis of Size-Controlled, Monodisperse, Freestanding Germanium Nanocrystals. *Appl. Phys. Lett.* **2007**, *91*, 093119.
- (13) Felbier, P.; Yang, J.; Theis, J.; Liptak, R. W.; Wagner, A.; Lorke, A.; Bacher, G.; Kortshagen, U. Highly Luminescent ZnO Quantum Dots Made in a Nonthermal Plasma. *Adv. Funct. Mater.* **2014**, 24, 1988–1993.
- (14) Thimsen, E.; Kortshagen, U. R.; Aydil, E. S. Nonthermal Plasma Synthesis of Metal Sulfide Nanocrystals from Metalorganic Vapor and Elemental Sulfur. *J. Phys. D: Appl. Phys.* **2015**, *48*, 314004.
- (15) Lin, P. A.; Sankaran, R. M. Plasma-Assisted Dissociation of Organometallic Vapors for Continuous, Gas-Phase Preparation of Multimetallic Nanoparticles. *Angew. Chem., Int. Ed.* **2011**, *50*, 10953–10956.
- (16) Kushner, M. J. The Empowerment of Plasma Modeling by Fundamental Electron Scattering Data. In *Bulletin of the American Physical Society*; American Physical Society: 2015; Vol. 60, p 9.
- (17) John, W. The Characteristics of Environmental and Laboratory-Generated Aerosols. In *Aerosol Measurement: Principles, Techniques, and Applications*; Willeke, K., Baron, P. A., Eds.; 1993; pp 54–76.
- (18) Johnson, E. O.; Malter, L. A Floating Double Probe Method for Measurements in Gas Discharges. *Phys. Rev.* **1950**, *80*, 58–68.
- (19) Grattan, K. T. V.; Palmer, A. W. Infrared Fluorescence "decaytime" Temperature Sensor. Rev. Sci. Instrum. 1985, 56, 1784–1787.
- (20) Kramida, A.; Ralchenko, Y.; Reader, J.; NIST ASD Team. NIST Atomic Spectra Database (ver. 5.3) http://physics.nist.gov/asd (accessed Jan 5, 2017).
- (21) Coburn, J. W.; Chen, M. Optical Emission Spectroscopy of Reactive Plasmas: A Method for Correlating Emission Intensities to Reactive Particle Density. *J. Appl. Phys.* **1980**, *51*, 3134–3136.
- (22) Wüst, K. Electron Temperature and Plasma Density of Capacitive Rf-discharges in Noble Gases. *Rev. Sci. Instrum.* **1992**, 63 (4), 2581–2583.

- (23) Daugherty, J. E.; Graves, D. B. Particulate Temperature in Radio Frequency Glow Discharges. *J. Vac. Sci. Technol., A* **1993**, *11*, 1126–1131.
- (24) Swinkels, G. H. P. M.; Kersten, H.; Deutsch, H.; Kroesen, G. M. W. Microcalorimetry of Dust Particles in a Radio-Frequency Plasma. *J. Appl. Phys.* **2000**, *88*, 1747–1755.
- (25) Lopez, T.; Mangolini, L. On the Nucleation and Crystallization of Nanoparticles in Continuous-Flow Nonthermal Plasma Reactors. J. Vac. Sci. Technol., B: Nanotechnol. Microelectron.: Mater., Process., Meas., Phenom. 2014, 32, 061802.
- (26) Mangolini, L.; Kortshagen, U. Selective Nanoparticle Heating: Another Form of Nonequilibrium in Dusty Plasmas. *Phys. Rev. E* **2009**, 79, 26405.
- (27) Allen, J. E. Probe Theory the Orbital Motion Approach. *Phys. Scr.* **1992**, *45*, 497–503.
- (28) Lampe, M.; Gavrishchaka, V.; Ganguli, G.; Joyce, G.; et al. Trapped Ion Effect on Shielding, Current Flow, and Charging of a Small Object in a Plasma. *Phys. Plasmas* **2003**, *10*, 1500–1513.
- (29) Khrapak, S. A.; Morfill, G. E. Grain Surface Temperature in Noble Gas Discharges: Refined Analytical Model. *Phys. Plasmas* **2006**, *13*, 104506.
- (30) Gatti, M.; Kortshagen, U. Analytical Model of Particle Charging in Plasmas over a Wide Range of Collisionality. *Phys. Rev. E* **2008**, 78, 46402.
- (31) Bohdansky, J.; Roth, J.; Bay, H. L. An Analytical Formula and Important Parameters for Low-energy Ion Sputtering. *J. Appl. Phys.* **1980**, *51*, 2861–2865.
- (32) Holland-Moritz, H.; Scheeler, S.; Stanglmair, C.; Pacholski, C.; Ronning, C. Enhanced Sputter Yields of Ion Irradiated Au Nano Particles: Energy and Size Dependence. *Nanotechnology* **2015**, *26*, 325301.
- (33) Nietiadi, M. L.; Sandoval, L.; Urbassek, H. M.; Möller, W. Sputtering of Si Nanospheres. *Phys. Rev. B: Condens. Matter Mater. Phys.* **2014**, *90*, 45417.
- (34) Sigmund, P. Sputtering by Ion Bombardment Theoretical Concepts. In *Sputtering by Particle Bombardment I*; Behrisch, R., Eckstein, W., Eds.; Springer: Berlin, 1981; pp 9–71.
- (35) Shen, C. Rarefied Gas Dynamics: Fundamentals, Simulations and Micro Flows; Springer: Berlin, 2005.
- (36) Helmersson, U.; Lattemann, M.; Bohlmark, J.; Ehiasarian, A. P.; Gudmundsson, J. T. Ionized Physical Vapor Deposition (IPVD): A Review of Technology and Applications. *Thin Solid Films* **2006**, *513*, 1–24.
- (37) Selwyn, G. S.; Heidenreich, J. E.; Haller, K. L. Particle Trapping Phenomena in Radio Frequency Plasmas. *Appl. Phys. Lett.* **1990**, *57*, 1876–1878.
- (38) Qin, Y.; Bilik, N.; Kortshagen, U. R.; Aydil, E. S. Laser Light Scattering from Silicon Particles Generated in an Argon Diluted Silane Plasma. *J. Phys. D: Appl. Phys.* **2016**, *49*, 085203.
- (39) Prost, W.; Kruis, F. E.; Otten, F.; Nielsch, K.; Rellinghaus, B.; Auer, U.; Peled, A.; Wassermann, E. F.; Fissan, H.; Tegude, F. J. Monodisperse Aerosol Particle Deposition: Prospects for Nanoelectronics. *Microelectron. Eng.* 1998, 41-42, 535–538.
- (40) Polarz, S.; Roy, A.; Merz, M.; Halm, S.; Schröder, D.; Schneider, L.; Bacher, G.; Kruis, F. E.; Driess, M. Chemical Vapor Synthesis of Size-Selected Zinc Oxide Nanoparticles. *Small* **2005**, *1*, 540–552.
- (41) Harra, J.; Mäkitalo, J.; Siikanen, R.; Virkki, M.; Genty, G.; Kobayashi, T.; Kauranen, M.; Mäkelä, J. M. Size-Controlled Aerosol Synthesis of Silver Nanoparticles for Plasmonic Materials. *J. Nanopart. Res.* **2012**, *14*, 870–880.
- (42) Lai, F. S.; Friedlander, S. K.; Pich, J.; Hidy, G. M. The Self-Preserving Particle Size Distribution for Brownian Coagulation in the Free-Molecule Regime. *J. Colloid Interface Sci.* **1972**, *39*, 395–405.
- (43) Talapin, D. V.; Rogach, A. L.; Haase, M.; Weller, H. Evolution of an Ensemble of Nanoparticles in a Colloidal Solution: Theoretical Study. *J. Phys. Chem. B* **2001**, *105*, 12278–12285.
- (44) Friedlander, S. K. The Characterization of Aerosols Distributed with Respect to Size and Chemical Composition—II. Classification

and Design of Aerosol Measuring Devices. J. Aerosol Sci. 1971, 2, 331–340.